PAPER

Check for updates

Synthesis of Pd-loaded mesoporous SnO2 hollow spheres for highly sensitive and stable methane gas sensors

Liping Yang, [ID][a] Zhou Wang,[a] Xinyuan Zhou,[ab] Xiaofeng Wu,[a] Ning Han[*ac] and Yunfa Chen[*ac]

High performance methane gas sensors have become more and more essential in different fields such as coal mining, kitchens and industrial production, which necessitates the design and synthesis of highly sensitive materials. Herein, mesoporous SnO_2 hollow spheres with high surface area (>90 m^2 g^{-1}) are prepared by a progressive inward crystallization routine, showing a high response of 1.31 to 250 ppm CH_4 at a working temperature of 400 °C. Furthermore, loading noble metal Pd onto the surface of SnO_2 hollow spheres by an adsorption–calcination process improves the response to 4.88 (250 ppm CH_4) at the optimal dosage of 1 wt% Pd. Meanwhile, the working temperature decreases to 300 °C, showing the prominent spillover effect of catalytic Pd and PdO−SnO$_2$ heterostructure sensitization as evidenced by the binding energy shift in the X-ray photoelectron spectroscopy (XPS) analysis. The response/recovery time is as short as 3/7 s and the sensitivity is stable for a test period as long as 15 weeks. All these performances show the promise of the highly porous Pd-loaded SnO$_2$ hollow spheres for high performance methane sensors.

Introduction

Methane (CH_4), a highly inflammable and explosive gas, is the major component of natural gas, coal mine tunnel gas and an important raw chemical for industrial applications. It is easy to cause an explosion, which can bring about great damage or disaster when the concentration is higher than 5% (in volume) in air.[1–4] In order to decrease the risk, a practicable technique is desired for detection of CH_4 at a low concentration to provide early alarm. On the other hand, CH_4 is difficult to detect *via* traditional methods due to its natural properties, such as being colorless, tasteless and odorless. Therefore, it is highly urgent to develop a convenient, rapid, effective and reliable sensor alarm to ensure the safety of life and property.

As a real-time measurement device, high performance and low power consumption gas sensors are an ideal choice. Especially, due to their excellent features,[5,6] semiconductor oxide gas sensors have attracted considerable attention such as SnO_2,[7–10] WO_3,[11,12] MoO_3,[13,14] In_2O_3,[15,16] ZnO,[17–19] Co_3O_4,[20,21] Fe_2O_3,[22,23]

VO_2,[24] Al_2O_3,[25] Ga_2O_3,[26] Cu_2O[27] and TiO_2 [28] *etc.* over the past few decades. It is noted that the sensing mechanism of semiconductor oxide gas sensors is based on directly detecting the chemi-resistance change of sensitive materials upon the adsorption and desorption of oxygen and redox reaction on the surface.[29–32] Therefore, the density of active sites on the surface is the key factor to determine the sensing performance. As is well known, the surface area has a great influence on the number of active sites. As a result, numerous efforts have been devoted to studying semiconductor oxide with large surface area in different unique structures. Among them, SnO_2, a typical n-type semiconductor, is extensively researched in view of the wide band gap (3.6 eV),[7] high mobility (160 cm^2 V^{-1} s)[33] and good chemical stability. For example, the ordered mesoporous SnO_2,[34] double-shelled SnO_2 nano-polyhedra,[35] Au-doped SnO_2 hollow multilayered sheets,[36] Pt-functionalized SnO_2 nano-flowers,[37] nanotubes,[38] Pd-doped SnO_2 hollow spheres,[39] cubic nanocages,[40] and hollow nanofibers[41] are helpful of detection limit, sensitivity, selectivity and response/recovery time. Although the gas sensing property has been dramatically improved, it still needs further improvements for the actual application due to the insufficient surface area of oxides, which are usually 30–50 m^2 g^{-1} by conventional ways in the literature reported.[42,43] Interestingly, the hollow structure with the inner and outer shell layer could enlarge the contact area between sensing materials and analyte gases. The high surface to volume ratio and density of surface active sites are favorable to the adsorption and desorption of gas molecules and interaction on

aState Key Laboratory of Multiphase Complex Systems, Institute of Process Engineering, Chinese Academy of Sciences, North Second Street 1, 100190 Beijing, P. R. China. E-mail: nhan@ipe.ac.cn

bUniversity of Chinese Academy of Sciences, No. 19A Yuquan Road, Beijing 100049, PR China

cCenter for Excellence in Regional Atmospheric Environment, Institute of Urban Environment, Chinese Academy of Sciences, Jimei Avenue 1799, 361021 Xiamen, P. R. China

the surface. Meanwhile, the hollow structure shortens the gas diffusion path and facilitates the gas molecules penetration.

Herein, this work introduces a simple strategy to synthesize Pd-loaded SnO_2 hollow spheres with high surface area (>90 m^2 g^{-1}). The Pd-loaded SnO_2 hollow spheres are prepared by two steps: first, the SnO_2 hollow spheres are fabricated through a novel *in situ* polymerization and subsequent progressive inward crystallization process. Second, Pd nanoparticles are loaded on the surface of SnO_2 hollow spheres with different amounts of Pd (0.1, 0.2, 0.5, 1 and 2 wt%) by adsorption and calcination. Interestingly, the Pd-loaded SnO_2 hollow spheres are composed of large amounts of sub-nanoparticles. And the BET surface area is higher than 90 m^2 g^{-1} and pore size distribution is 2–7 nm, suitable for CH_4 molecules transport. Moreover, the strong spillover effect of Pd nanoparticles and PdO–SnO_2 heterogeneous sensitization are beneficial to gas sensing performance. The results display Pd-loaded SnO_2 hollow spheres with low working temperature (300 °C), high response (4.88 to 250 ppm), fast response/recovery time (3/7 s for 250 ppm), excellent selectivity and long-term (>15 weeks) stability towards CH_4 gas, showing the promise of Pd-loaded SnO_2 hollow spheres for CH_4 leakage alarm.

Experimental

Chemicals and reagents

Tin(IV) isopropoxide ($Sn(OC_3H_7)_4$, 98%) and sodium tetra-chloropalladate (Na_2PdCl_4, >99.9%) are supplied by Alfa Aesar. Hydrochloric acid (HCl, 37%), urea ($CO(NH_2)_2$) and formaldehyde (HCHO, 37%) are purchased from Sinopharm Chemical Reagent Co., Ltd. All analytical chemical reagents are used directly without further purification.

Preparation of pure SnO_2 hollow spheres

The urea–formaldehyde (UF) synthetical process followed here is referenced as previous reported.[44,45] In a typical synthesis, 30 mL of deionized water, 1 mL of hydrochloric acid and 10 mmol of tin(IV) isopropoxide are magnetic stirred at 60 °C until the mixture become yellow sol. Subsequently, the sol is cooled down and stored for further use. Then, 10 mL of SnO_2 sol, 30 mL of deionized water and 1 g of urea are mixed under magnetic stirring. The pH of mixture is controlled at 1–1.5 by hydrochloric acid and then 2 mL of formaldehyde (37 wt%) is added under violent stirring. Finally, the reaction solution is static for 3 h at room temperature. The precipitate is collected by centrifugation, washed with deionized water and ethanol for several times, respectively and dried at 80 °C overnight for further characterization. After annealing at 500 °C for 2 h in tube furnace under air atmosphere, the pure SnO_2 hollow spheres are formed.

Preparation of Pd-loaded SnO_2 hollow spheres

The Pd-loaded SnO_2 hollow spheres are prepared by adsorption–calcination process. In a typical synthesis procedure, 100 mg of SnO_2 hollow spheres is added into 30 mL of ethanol and ultrasonicated for several minutes. Then, the given quantity

of Na_2PdCl_4 is added and stirred for 12 h. The powder is collected by centrifugation and rinsed several times with deionized water and ethanol to remove impurities. After that, the Pd-loaded SnO_2 hollow spheres are formed during calcination at 500 °C for 2 h in air.

Materials characterization

The morphology and structure features are investigated by FESEM (JEOL JSM-6700F, 10 kV, 10 μA). More detailed crystallinity and component distribution information are acquired through TEM (JEOL-2100F, 200 kV) and energy-dispersive X-ray (EDX) analysis, respectively. The crystalline structure is examined by the powder X-ray diffraction (XRD, Panalytical X'pert PRO system, 40 kV, 40 mA, Cu K_α radiation, $\lambda = 1.5406$ Å). The chemical state of elements is measured by the X-ray photoelectron spectroscopy (XPS, XLESCALAB 250Xi, Al-K_α radiation source, C 1s peak at 284.8 eV). The surface area is characterized by the N_2 adsorption–desorption isotherms on an automatic surface analyser (SSA-7300) at 77 K.

Fabrication and measurement of the gas sensor

The gas sensors employ pure SnO_2 and Pd-loaded SnO_2 hollow spheres as sensitive materials. The detailed fabrication procedures are as follows: the given quantity of powders (pure and Pd-loaded SnO_2 hollow spheres) are dispersed into ethanol to form a homogenous slurry. Afterwards, the well-dispersed paste is drop-casted onto the rectangle plane with a length of 1 mm and 2 mm (red area), which consists of electrode and Pt wires on each angle (Fig. 1a). The working temperature is controlled by employing a pair of Pt wires as a heater (yellow area). The other pair is used as conducting wires to measure the resistance change. Subsequently, the sensor devices with coated sensing materials is dried and aged at 300 °C for 12 h to ensure the ohmic metallic contacts with electrode. It is noted that more than two devices are prepared per material to collect the sensing performance for reducing the deviation caused by the different devices. Finally, the gas sensing characteristics are performed on a static test system (Winsen Instruments Co. Ltd., Zhengzhou, China) with a chamber of 18 L. In the testing system (Fig. 1b), the circuit voltage (V_c) is set at 5 V, and the output voltage (V_L) is set as the voltage of load resistance (R_L). During the testing process, the sensor devices are placed into the chamber filled with air, and the target gases are injected into
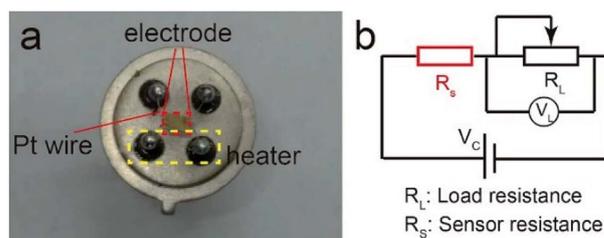

Fig. 1 (a) The photograph of typical gas sensor device, (b) the diagram of the electric circuit for gas sensing measurement.

the chamber *via* a syringe. The cover of chamber is removed when V_L reaches a constant value.

The response of the sensor devices is defined as the ratio of resistance, $S = R_a/R_g$ (n-type), $S = R_g/R_a$ (p-type), where R_a is the resistance value of gas sensor in the air, and R_g is the resistance value in the analyte gases. The response/recovery time is determined as the time required to reach 90% of the total resistance change after the sensor is exposed to the target gas and air, respectively.

Results and discussion

Structural and morphological characterization

The fabrication procedure of Pd-loaded SnO_2 hollow spheres are as follows. Firstly, the SnO_2 sol is prepared by hydrolysis of tin(IV) isopropoxide (seeing Experimental section). Then, with the proceeding of *in situ* polymerization and progressive inward crystallization process of SnO_2 colloids, pure SnO_2 hollow spheres are formed. Finally, Pd-loaded SnO_2 hollow spheres are prepared by a simple adsorption and calcination process. Fig. 2a shows the SnO_2–UF microspheres precursor are regularly spherical shape with narrow distribution and the diameter is about 1.5 μm. The high-magnification FESEM image (inset of Fig. 2a) demonstrates that it consists of sub-particles and the surface is rough. After heat treatment in air, pure SnO_2 sample maintains similar morphology to that of precursor, as shown in Fig. 2b. As can be seen, the pure SnO_2 powder is uniform sphere in shape and rough surface. The statistics of particle size shows the diameter mainly at 0.9 μm. Furthermore, TEM image of pure SnO_2 powder (Fig. 2c) illustrates obvious void space in the interior from dramatical contrast of brightness and darkness, confirming the hollow structure feature.

The morphological structure of Pd-loaded SnO_2 hollow spheres is investigated by using FESEM and TEM technique. Fig. 3a shows Pd-loaded SnO_2 hollow spheres are analogous to pure SnO_2 hollow spheres. It is well-defined spherical shape and uniform particle size with the diameter of 0.9 μm. The TEM image (Fig. 3b) demonstrates the clear hollow structure. Apart from that, the edge of Pd-loaded hollow sphere is much harsher than pure SnO_2 hollow spheres, illustrating Pd nanoparticles have been successfully adsorbed onto the surface. The HRTEM image (inset of Fig. 3b) shows Pd-loaded SnO_2 hollow spheres are high crystallization and the lattice fringe is 0.337 nm, well indexed with the (110) plane of cassiterite SnO_2 (JCPDS no. 41-1445). Although no obvious Pd particles can be found, Pd does exist as evidenced by EDX mapping scanning images in Fig. 3c, which further confirm that the elements of Sn, O and Pd
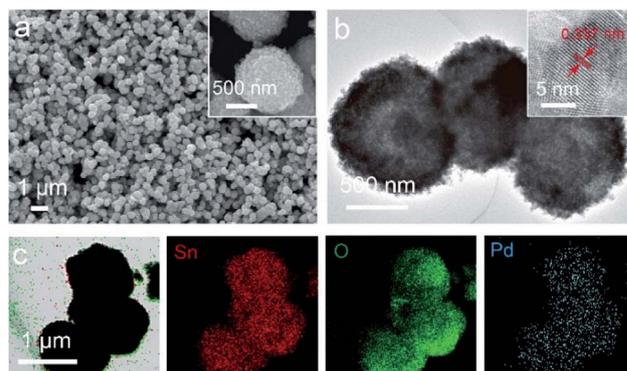

Fig. 3 (a) FESEM image, (b) TEM image and (c) EDX analysis of Pd-loaded SnO_2 hollow spheres.

distribute uniformly over the whole shell of hollow spheres, as shown in the color of red, green and cyan. Therefore, the existence of Pd would be in atomic or cluster, which would be favorable for highly active surface catalytic reaction.

The crystallization and phase purity of Pd-loaded SnO_2 hollow spheres with different amounts of Pd (pure, 0.1 wt%, 0.2 wt%, 0.5 wt%, 1 wt% and 2 wt%) are characterized by XRD pattern. Fig. 4 shows XRD pattern of Pd-loaded SnO_2 hollow spheres with Pd contents of pure, 0.1, 0.2, 0.5, 1 and 2 wt%, respectively. The main diffraction peaks for each sample are in good agreement with the cassiterite SnO_2 phase (JCPDS no. 41-1445), confirming the result of HRTEM (Fig. 3b). No other characteristic impurity phase peaks can be observed for each sample. Furthermore, no obvious diffraction peaks are ascribed to Pd or PdO because the trace amount and small crystalline size are difficult to detect by XRD analysis, which is similar to the reported Pd–SnO_2 microspheres,[39] Pt–SnO_2 microspheres,[43] Au–MoO_3 hierarchical hollow spheres.[13]

On the other hand, the surface chemical composition of each element is investigated by XPS analysis. Fig. 5a shows XPS

Fig. 2 (a) FESEM image of SnO_2–UF microspheres precursor, (b) FESEM and (c) TEM image of pure SnO_2 hollow spheres.
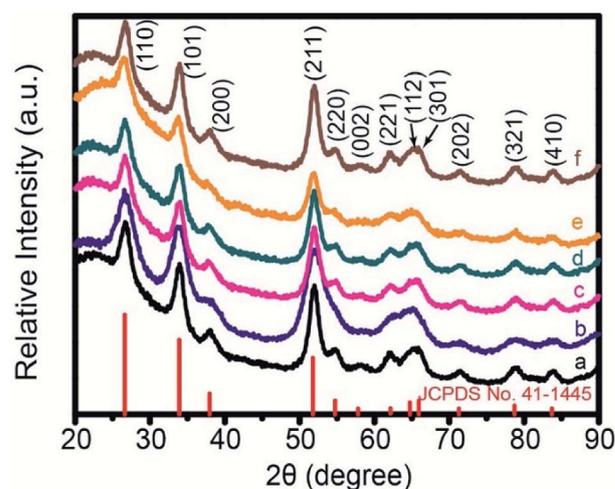

Fig. 4 XRD pattern of Pd-loaded SnO_2 hollow spheres with Pd amount of (a) pure, (b) 0.1 wt%, (c) 0.2 wt%, (d) 0.5 wt%, (e) 1 wt% and (f) 2 wt%, respectively.
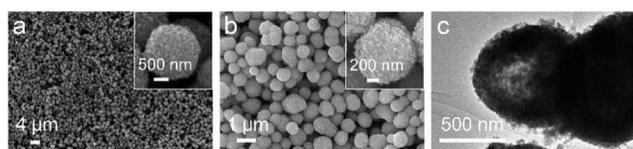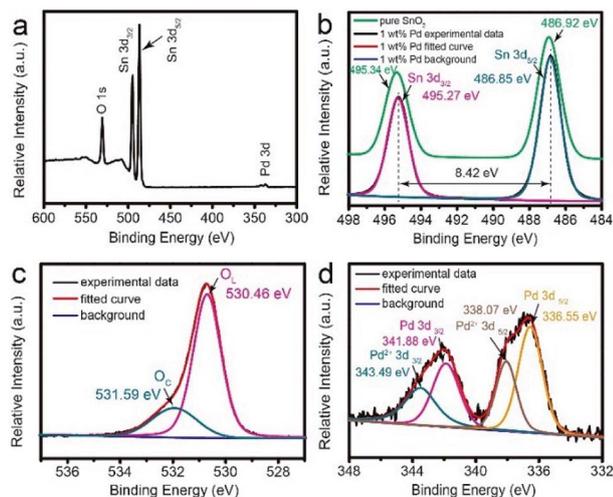
Fig. 5 XPS analysis for 1 wt% Pd-loaded SnO₂ hollow spheres: (a) survey spectra, high resolution spectra of (b) Sn 3d, (c) O 1s and (d) Pd 3d.

survey spectra of 1 wt% Pd-loaded SnO_2 hollow spheres. Obviously, there are Sn, O and Pd in the plot and no other peaks are observed. It is noted that the intensity of Pd is extremely weak due to the low decorating content, illustrated by XRD (Fig. 4). In the spectra of Sn 3d (Fig. 5b), the symmetric binding energy peaks of 495.27 eV and 486.85 eV are ascribed to Sn $3d^{3/2}$ and $3d^{5/2}$, respectively, which is attributed to Sn^{4+} of SnO_2. The binding energy difference of these two peaks is 8.42 eV, in consistent with the literature reported value.[43,46] However, the spectra of Sn 3d for pure SnO_2 hollow spheres (green line) shows the corresponding binding energy peaks are located at 495.34 eV and 486.92 eV, respectively. This slight movement indicates strong interaction between SnO_2 and Pd nanoparticles, which is beneficial to improve gas sensing performance. Fig. 5c illustrates that the peak of O 1s could be separated into two fitted peaks (magenta line and cyan line), indicating the significant difference for the oxygen states on the surface. The peak located at 530.46 eV is assigned to the lattice oxygen (O_L) species, which could not react with analyte gases at low temperature. Hence, the O_L species have no significant influence on gas sensing property. However, the other binding energy peak positioned at 531.59 eV is indexed to the chemisorbed oxygen (O_C) species, such as O_2^-, O^- and O^{2-} ions.[21] These chemisorbed ions could interact with target gas and increase the electron concentration on the sensing material surface, which is favorable for gas sensing performance. In the spectra of Pd 3d (Fig. 5d), the binding energy peak is decomposed into two pairs. One pair peaks of Pd^{2+} $3d^{3/2}$ and Pd^{2+} $3d^{5/2}$ locate at 343.49 eV and 338.07 eV, respectively, confirming the formation of PdO–SnO_2 heterogeneous.[47] The other pair appeared at 341.88 eV and 336.55 eV are attributed to Pd $3d^{3/2}$ and Pd $3d^{5/2}$, respectively, indicating that Pd nanoparticles exists in the form of metallic Pd. The spillover effect of Pd nanoparticles could promote the interaction with sensitive material surface. Thus, it will dramatically impact the gas sensing performance.
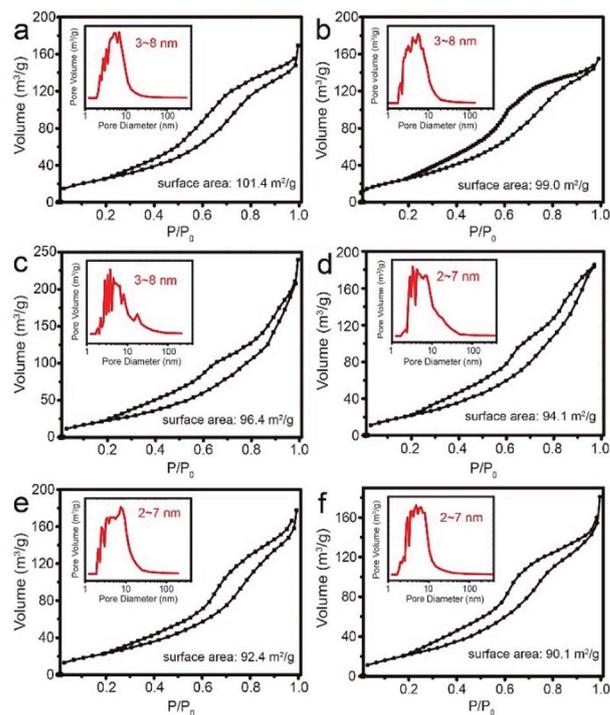

Fig. 6 N₂ adsorption–desorption isotherms of Pd-loaded SnO₂ hollow spheres with different Pd amount: (a) pure, (b) 0.1 wt%, (c) 0.2 wt%, (d) 0.5 wt%, (e) 1 wt% and (f) 2 wt%, respectively. The inset of each sample is pore size.

Furthermore, N_2 adsorption–desorption isotherm analysis shows the surface area and pore size distribution. The plots show obvious hysteresis loop for each sample, as shown in Fig. 6, illustrating the existence of pore. As can be observed, the surface area is 101.4 m^2 g^{-1} for pure SnO_2 hollow spheres (Fig. 6a), while it decreases a little bit to 90.1 m^2 g^{-1} for 2 wt% Pd-loaded SnO_2 (Fig. 6f). The reduction may be resulted from Pd or PdO nanoparticles take up the space of pore channel. The pore size distribution (inset of Fig. 6) for each sample is broad and mainly concentrated on the range of 2–7 nm, which is suitable for diffusion and transport of CH_4 molecules. The large surface area and optimum pore size play an important role in improving gas sensing property.

Methane gas sensing behavior

The working temperature plays an important role in enhancing gas sensing performance. Fig. 7 shows the temperature-dependent property of gas sensor based on different amount of Pd-loaded SnO_2 hollow spheres toward 250 ppm CH_4. As can be seen, the response continues increase for pure SnO_2, 0.1 wt%, 0.2 wt% and 0.5 wt% Pd-loaded SnO_2 hollow spheres as the operating temperature increases from 240 °C to 400 °C. At the same time, these sensor devices show relatively low sensitivity. For instance, when the temperature is up to 400 °C, the highest response is only 2.35 for 0.5 wt% Pd-loaded SnO_2 hollow spheres sensor. For 1 wt% and 2 wt% Pd-loaded SnO_2 hollow spheres, however, the temperature-dependence plots show
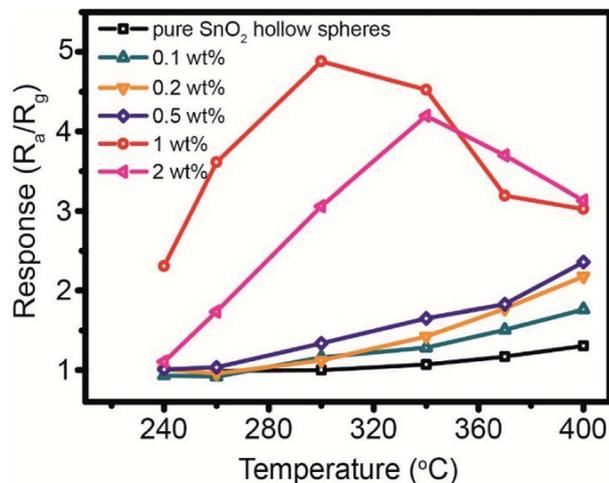
Fig. 7 The response of Pd-loaded SnO_2 hollow spheres with different amounts of Pd (pure, 0.1 wt%, 0.2 wt%, 0.5 wt%, 1 wt% and 2 wt%) toward CH_4 with a concentration of 250 ppm at different working temperature (R_a: the resistance value of gas sensor in the air; R_g: the resistance value in CH_4 gas).

Fig. 8 The dynamic response curve based on 1 wt% Pd-loaded SnO_2 hollow spheres sensor toward 250 ppm CH_4 at 300 °C.

"increase-maximum-decrease" tendency over the temperature range of 240–400 °C. Obviously, the response reaches the maximum when the working temperature increases to 300 °C and 340 °C. The corresponding response value is 4.88 and 4.20, respectively, almost four times that of pure SnO_2 hollow spheres (1.31). Taking the cost and energy consumption into account, the optimal working temperature of 300 °C and 1 wt% Pd-loaded SnO_2 hollow spheres are applied in the subsequent application.

The response/recovery time is another significant parameter for evaluating sensor performance. Fig. 8 shows the response time and recovery time of 1 wt% Pd-loaded SnO_2 hollow spheres sensor are 3 s and 7 s, respectively, much lower than that of literature reported.[47] The short response/recovery time indicates that it could detect CH_4 as quickly as possible in real-time application. It is attributed to the unique hollow structure, strong spillover effect of Pd nanoparticles and PdO–SnO_2 heterogeneous sensitization, affecting the density of active sites and electron concentration on the surface.

Fig. 9a shows the typical response curve of 1 wt% Pd-loaded SnO_2 hollow spheres sensor toward different CH_4 concentration from 25 to 1000 ppm. As can be seen, the response of sensor is 1.86 when the concentration of CH_4 is only 25 ppm, indicating lower detection limit. With the concentration increasing, the response increases to 2.25 for 50 ppm, 2.98 for 100 ppm, 4.89 for 250 ppm, 6.35 for 500 ppm, 7.32 for 750 ppm and 7.89 for 1000 ppm, respectively. The corresponding relationship between concentration and response (Fig. 9b) is linear, especially from 25 to 250 ppm. The correlative coefficient R^2 is 0.99769. The good linear relationship shows 1 wt% Pd-loaded SnO_2 hollow spheres sensor can real-time, effectively, rapidly monitor CH_4 in kitchen and coal mine.

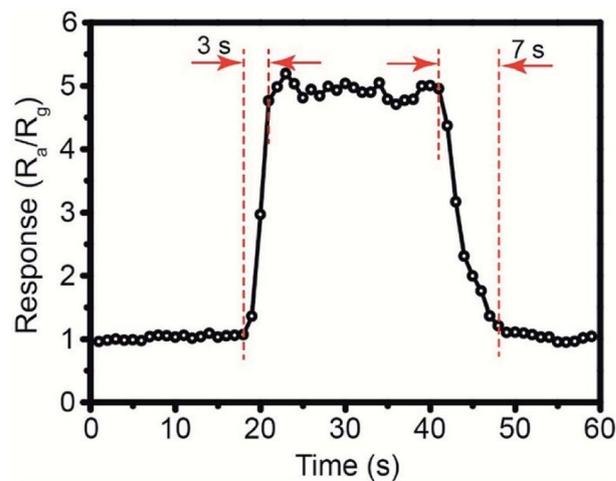To verify the reliable reproducibility, Fig. 9c displays the 1 wt% Pd-loaded SnO_2 hollow spheres sensor exposed to

250 ppm CH_4 under 7 successive cycles at 300 °C. This sensor exhibits repeatable and stable resistance change with a response of 4.89 (Fig. 9c). It is noted that the resistance maintains at a constant value of 148.5 kΩ, illustrating lower energy consumption. In addition, the long-term stability of sensor based on 1 wt% Pd-loaded SnO_2 hollow spheres is also investigated (Fig. 9d). After 15 weeks testing, the response nearly keeps at a constant value, demonstrating excellent long-term stability.

In addition, the selectivity of the 1 wt% Pd-loaded SnO_2 hollow spheres sensor is investigated by exposed to different gases, including formaldehyde, benzene, toluene, humidity and methane, which are usual gases in kitchen or coal mine.
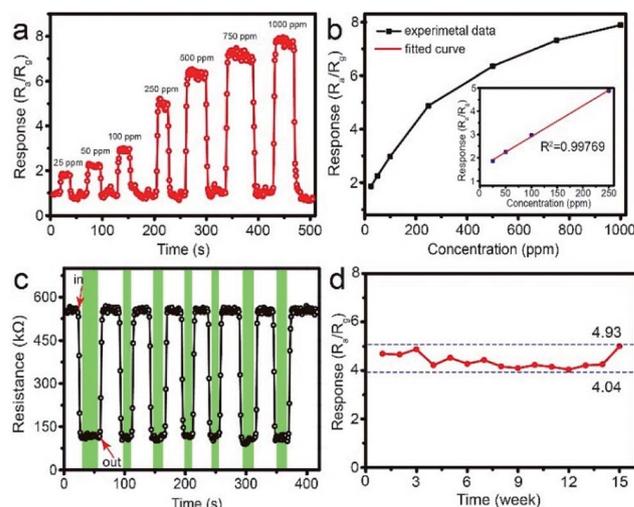

Fig. 9 The gas sensing performance of 1 wt% Pd-loaded SnO_2 hollow spheres sensor: (a) the response curve toward different CH_4 concentration, (b) the corresponding linear fitting curve between concentration and response, (c) dynamic resistance curve toward 250 ppm CH_4 under 7 cycles, (d) the response toward 250 ppm CH_4 for long-term cyclic tests. The operating temperature is 300 °C.
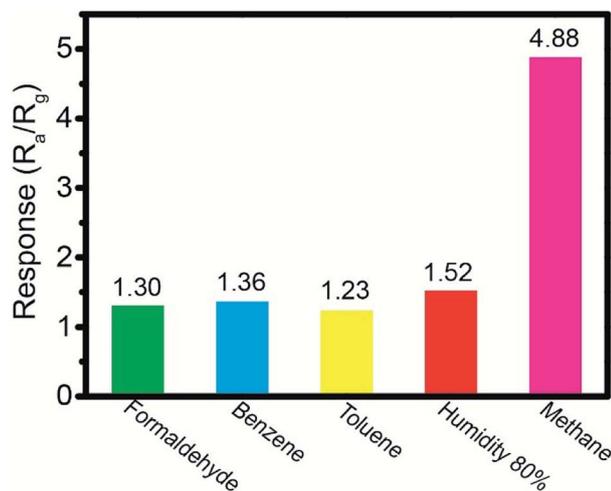
Fig. 10 The selectivity of the 1 wt% Pd-loaded SnO$_2$ hollow spheres sensor toward different gases, including 1 ppm of formaldehyde, benzene, toluene, 80% RH and 250 ppm of methane.

As shown in Fig. 10, the 1 wt% Pd-loaded SnO$_2$ hollow spheres sensor shows a high response of 4.88 to CH$_4$ (250 ppm), clear much higher than other typical gases (1.30 for 1 ppm formaldehyde, 1.36 for 1 ppm benzene, 1.23 for 1 ppm toluene and 1.52 for 80% RH), illustrating the excellent selectivity. Due to the concentration of interference gases is lower than 1 ppm in kitchen or coal mine, 1 ppm is used to evaluate the selectivity.

The gas sensing property of pure SnO$_2$ hollow spheres sensor, 1 wt% Pd-loaded SnO$_2$ hollow spheres sensor and literature reported are summarized in Table 1. Clearly, this work shows excellent CH$_4$ sensing performance than those of previously reported. Therefore, 1 wt% Pd-loaded SnO$_2$ hollow spheres sensor would be the best candidate for detecting CH$_4$ in practical application.
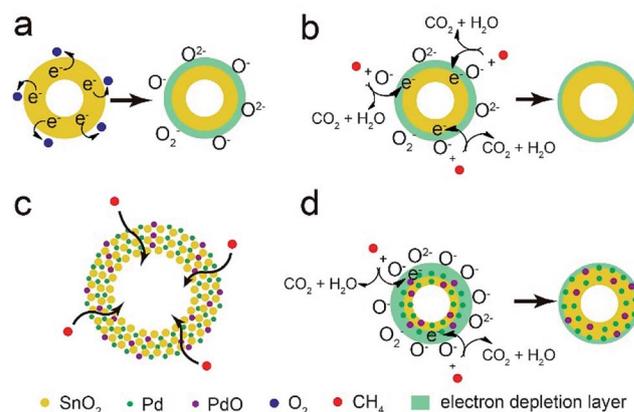

Fig. 11 The schematic illustration of CH$_4$ sensing mechanism for pure SnO$_2$ (a and b) and Pd-loaded SnO$_2$ hollow spheres (c and d).

Mechanism discussion

The CH$_4$ sensor is based on the chemi-resistivity change of Pd-loaded SnO$_2$ hollow spheres. When it is exposed to air ambient (Fig. 11a), oxygen molecule could attract electron from SnO$_2$ and adsorb on the surface of sensing materials in the form of chemisorbed oxygen ions (O$^-$, O^{2-} and O$_2^-$), which results in the formation of electron depletion layer and resistance increase. The following reactions are shown in eqn (1)–(3).

$$O_2 + e^- \rightarrow O_2^- \qquad (1)$$
$$O_2^- + e^- \rightarrow O^- \qquad (2)$$
$$O^- + e^- \rightarrow O^{2-} \qquad (3)$$
$$CH_4 + 4O^- \rightarrow CO_2 + 2H_2O + 4e^- \qquad (4)$$

Table 1 The brief summary of sensing performance of CH$_4$ sensors based on SnO$_2$

Year	Materials	Working temperature/°C	Concentration/ppm	Response	Response/recovery time/s	Ref.
2000	Pt–SnO$_2$	350	500	21%[b]	—	49
2002	Pd–SnO$_2$	350	1000	35%[b]	—	50
2005	Fe–SnO$_2$	350	1000	65%[b]	—	51
2005	Pt–Ca/SnO$_2$	400	5000	2.3[c]	—	52
2006	Fe–SnO$_2$	350	1000	70%[c]	—	53
2010	SnO$_2$	600	4000	1.6[b]	—	54
2011	SnO$_2$–Pd	400	6600	20%[b]	—	55
2012	Pd–SnO$_2$	220	200	97.2%[b]	26/70	56
2013	ZnO–SnO$_2$	350	5000	80%[b]	—	57
2014	Ni$_2$O$_3$–SnO$_2$	400	200	127%[a]	—	58
2015	Ag–SnO$_2$	430	2000	75%[b]	—	59
2017	Pd/SnO$_2$-rGO	RT	12000	9.5%[b]	300/420	60
2018	Pt–SnO$_2$	350	1000	4.4825[c]	24.3/141.1	48
	SnO$_2$	400	250	1.31[c]	4/9	This work
	Pd–SnO$_2$	300	250	4.88[c]	3/7	This work

[a] $R_a/R_g \times 100\%$. [b] $(R_a - R_g)/R_g \times 100\%$. [c] R_a/R_g.

When it exposed to CH_4 gas (Fig. 11b), CH_4 molecules could react with the chemisorbed oxygen species on the surface of SnO_2 and release electron back to the conduction band (eqn (4)),[56,61,62] causing the reduction of electron depletion layer and resistance.

According to XPS analysis (Fig. 5d), the element of Pd appears in the form of Pd and PdO nanoparticles. And these nanoparticles are well-dispersed on the surface of SnO_2 hollow spheres from EDX analysis (Fig. 3c). The improved CH_4 sensing performance could be explained by two aspects: (i) unique hollow structure and (ii) the spillover effect of Pd nanoparticles and $PdO–SnO_2$ heterogeneous sensitization. The 1 wt% Pd-loaded SnO_2 hollow spheres with high surface area (92.4 m^2 g^{-1}) provides abundant active sites on the outer and inner surface and high porosity facilitates CH_4 molecules diffusion and transport (Fig. 11c). Furthermore, due to the strong spillover effect of Pd nanoparticles, the oxygen molecules could easily dissociate into chemisorbed oxygen species and adsorb on the surface, resulting in more active sites on the surface of $Pd–SnO_2$ than that of pure SnO_2, which would attract more electron from $Pd–SnO_2$ to form wider electron depletion layer (Fig. 11d). On the other hand, $PdO–SnO_2$ heterogeneous structure also promotes the sensing activity. Therefore, the $Pd–SnO_2$ hollow spheres sensor shows excellent CH_4 sensing property.

Conclusions

In summary, this work reports a simple, rapid, effective and reliable CH_4 sensor based on Pd-loaded SnO_2 hollow spheres, which are fabricated through two steps: pure SnO_2 hollow spheres by a novel routine and Pd loading by adsorption–calcination process. Typically, the unique structure with high surface area and porosity provides large number of active sites, which is good for gas sensing performance. In addition, taking the advantage of spillover effect of catalytic Pd and $PdO–SnO_2$ heterostructure sensitization, the sensor based on Pd-loaded SnO_2 hollow spheres exhibits superior CH_4 sensing behavior. Compared to pure SnO_2 one, 1 wt% Pd-loaded SnO_2 hollow spheres sensor shows low working temperature (300 °C), high sensitivity (4.88 for 250 ppm), fast response/recovery time (3/7 s to 250 ppm), excellent selectivity and reliable stability (>15 weeks). The Pd-loaded SnO_2 hollow spheres sensing materials have potential promise for CH_4 sensor alarm.

Conflicts of interest

There are no conflicts to declare.

Acknowledgements

Notes and references

1 Y. Cao, J. Zhao, X. Zou, P.-P. Jin, H. Chen, R. Gao, L.-J. Zhou, Y.-C. Zou and G.-D. Li, RSC Adv., 2015, 5, 5424–5431.
2 W. Lu, G. Jing, X. Bian, H. Yu and T. Cui, Sens. Actuators, A, 2016, 242, 9–17.
3 K. Wetchakun, T. Samerjai, N. Tamaekong, C. Liewhiran, C. Siriwong, V. Kruefu, A. Wisitsoraat, A. Tuantranont and S. Phanichphant, Sens. Actuators, B, 2011, 160, 580–591.
4 D. Zhang, N. Yin and B. Xia, J. Mater. Sci.: Mater. Electron., 2015, 26, 5937–5945.
5 H.-J. Kim and J.-H. Lee, Sens. Actuators, B, 2014, 192, 607–627.
6 J.-H. Lee, Sens. Actuators, B, 2009, 140, 319–336.
7 X. Han, M. Jin, S. Xie, Q. Kuang, Z. Jiang, Y. Jiang, Z. Xie and L. Zheng, Angew. Chem., 2009, 48, 9180–9183.
8 Y. Li, L. Qiao, D. Yan, L. Wang, Y. Zeng and H. Yang, J. Alloys Compd., 2014, 586, 399–403.
9 J.-g. Kang, J.-S. Park and H.-J. Lee, Sens. Actuators, B, 2017, 248, 1011–1016.
10 L. Xiao, S. Shu and S. Liu, Sens. Actuators, B, 2015, 221, 120–126.
11 Y. Zhu, Y. Zhao, J. Ma, X. Cheng, J. Xie, P. Xu, H. Liu, H. Liu, H. Zhang, M. Wu, A. A. Elzatahry, A. Alghamdi, Y. Deng and D. Zhao, J. Am. Chem. Soc., 2017, 139, 10365–10373.
12 Y. Li, W. Luo, N. Qin, J. Dong, J. Wei, W. Li, S. Feng, J. Chen, J. Xu, A. A. Elzatahry, M. H. Es-Saheb, Y. Deng and D. Zhao, Angew. Chem., 2014, 53, 9035–9040.
13 L. Sui, X. Zhang, X. Cheng, P. Wang, Y. Xu, S. Gao, H. Zhao and L. Huo, ACS Appl. Mater. Interfaces, 2017, 9, 1661–1670.
14 F. Ji, X. Ren, X. Zheng, Y. Liu, L. Pang, J. Jiang and S. F. Liu, Nanoscale, 2016, 8, 8696–8703.
15 A. Shanmugasundaram, V. Gundimeda, T. Hou and D. W. Lee, ACS Appl. Mater. Interfaces, 2017, 9, 31728–31740.
16 T. Waitz, T. Wagner, T. Sauerwald, C.-D. Kohl and M. Tiemann, Adv. Funct. Mater., 2009, 19, 653–661.
17 W. T. Koo, S. J. Choi, S. J. Kim, J. S. Jang, H. L. Tuller and I. D. Kim, J. Am. Chem. Soc., 2016, 138, 13431–13437.
18 N. Han, X. Wu, D. Zhang, G. Shen, H. Liu and Y. Chen, Sens. Actuators, B, 2011, 152, 324–329.
19 V. Galstyan, E. Comini, I. Kholmanov, G. Faglia and G. Sberveglieri, RSC Adv., 2016, 6, 34225–34232.
20 J. Tan, J. Dun, L. Li, J. Zhao, W. Tan, Z. Lin and X. Huang, Sens. Actuators, B, 2017, 249, 44–52.
21 W. T. Koo, S. Yu, S. J. Choi, J. S. Jang, J. Y. Cheong and I. D. Kim, ACS Appl. Mater. Interfaces, 2017, 9, 8201–8210.
22 M. Dai, L. Zhao, H. Gao, P. Sun, F. Liu, S. Zhang, K. Shimanoe, N. Yamazoe and G. Lu, ACS Appl. Mater. Interfaces, 2017, 9, 8919–8928.
23 S. Liang, J. Li, F. Wang, J. Qin, X. Lai and X. Jiang, Sens. Actuators, B, 2017, 238, 923–927.
24 A. K. Prasad, S. Amirthapandian, S. Dhara, S. Dash, N. Murali and A. K. Tyagi, Sens. Actuators, B, 2014, 191, 252–256.
25 F. Liu, Y. Zhang, Y. Yu, J. Xu, J. Sun and G. Lu, Sens. Actuators, B, 2011, 160, 1091–1097.

26 M. Fleischer and H. Meixner, *Sens. Actuators, B*, 1995, **24–25**, 544–547.

27 Z. Xie, N. Han, W. Li, Y. Deng, S. Gong, Y. Wang, X. Wu, Y. Li and Y. Chen, *Phys. Status Solidi A*, 2017, **214**, 1600904.

28 J. Li, X. Li, Q. Zhao, Z. Jiang, M. Tadé, S. Wang and S. Liu, *Sens. Actuators, B*, 2018, **255**, 133–139.

29 M. Makoto Egashira, Y. Shimizu, Y. Takao and S. Sako, *Sens. Actuators, B*, 1996, 35–36.

30 D. E. Williams, *Sens. Actuators, B*, 1999, **57**, 1–16.

31 N. Yamazoe, G. Sakai and K. Shimanoe, *Catal. Surv. Asia*, 2003, **7**, 63–75.

32 C. Wang, L. Yin, L. Zhang, D. Xiang and R. Gao, *Sensors*, 2010, **10**, 2088–2106.

33 S. J. Choi, M. P. Kim, S. J. Lee, B. J. Kim and I. D. Kim, *Nanoscale*, 2014, **6**, 11898–11903.

34 X. Xiao, L. Liu, J. Ma, Y. Ren, X. Cheng, Y. Zhu, D. Zhao, A. A. Elzatahry, A. Alghamdi and Y. Deng, *ACS Appl. Mater. Interfaces*, 2018, **10**, 1871–1880.

35 Y. Bing, Y. Zeng, C. Liu, L. Qiao and W. Zheng, *Nanoscale*, 2015, **7**, 3276–3284.

36 Y. Bing, Y. Zeng, S. Feng, L. Qiao, Y. Wang and W. Zheng, *Sens. Actuators, B*, 2016, **227**, 362–372.

37 Y. Liu, J. Huang, J. Yang and S. Wang, *Solid-State Electron.*, 2017, **130**, 20–27.

38 P. M. Bulemo, H. J. Cho, N. H. Kim and I. D. Kim, *ACS Appl. Mater. Interfaces*, 2017, **9**, 26304–26313.

39 Q. Wang, X. Li, F. Liu, C. Liu, T. Su, J. Lin, P. Sun, Y. Sun, F. Liu and G. Lu, *RSC Adv.*, 2016, **6**, 80455–80461.

40 L. Qiao, Y. Bing, Y. Wang, S. Yu, Z. Liang and Y. Zeng, *Sens. Actuators, B*, 2017, **241**, 1121–1129.

41 J.-K. Choi, I.-S. Hwang, S.-J. Kim, J.-S. Park, S.-S. Park, U. Jeong, Y. C. Kang and J.-H. Lee, *Sens. Actuators, B*, 2010, **150**, 191–199.

42 J. Huang, L. Wang, C. Gu, M. Zhai and J. Liu, *CrystEngComm*, 2013, **15**, 7515.

43 Y. Li, D. Deng, N. Chen, X. Xing, X. Xiao and Y. Wang, *RSC Adv.*, 2016, **6**, 83870–83879.

44 L. P. Yang, X. J. Lin, X. Zhang, W. Zhang, A. M. Cao and L. J. Wan, *J. Am. Chem. Soc.*, 2016, **138**, 5916–5922.

45 L. L. Hu, L. P. Yang, D. Zhang, X. S. Tao, C. Zeng, A. M. Cao and L. J. Wan, *Chem. Commun.*, 2017, **53**, 11189–11192.

46 C. Dong, X. Liu, X. Xiao, G. Chen, Y. Wang and I. Djerdj, *J. Mater. Chem. A*, 2014, **2**, 20089–20095.

47 K. Zhang, X. Yang, Y. Wang, Y. Bing, L. Qiao, Z. Liang, S. Yu, Y. Zeng and W. Zheng, *Sens. Actuators, B*, 2017, **243**, 465–474.

48 W. Lu, D. Ding, Q. Xue, Y. Du, Y. Xiong, J. Zhang, X. Pan and W. Xing, *Sens. Actuators, B*, 2018, **254**, 393–401.

49 A. A. Cabot, J. Arbiol, J. R. Morante, U. Weimar, N. Barsan and W. Gopel, *Sens. Actuators, B*, 2000, **70**, 87–100.

50 A. Cabot, A. Vila and J. R. Morant, *Sens. Actuators, B*, 2002, **84**, 12–20.

51 S. Bose, S. Chakraborty, B. K. Ghosh, D. Das, A. Sen and H. S. Maiti, *Sens. Actuators, B*, 2005, **105**, 346–350.

52 B.-K. Min and S.-D. Choi, *Sens. Actuators, B*, 2005, **108**, 119–124.

53 S. Chakraborty, A. Sen and H. S. Maiti, *Sens. Actuators, B*, 2006, **115**, 610–613.

54 T. Waitz, B. Becker, T. Wagner, T. Sauerwald, C. D. Kohl and M. Tiemann, *Sens. Actuators, B*, 2010, **150**, 788–793.

55 T. Wagner, M. Bauer, T. Sauerwald, C. D. Kohl and M. Tiemann, *Thin Solid Films*, 2011, **520**, 909–912.

56 D. Haridas and V. Gupta, *Sens. Actuators, B*, 2012, **166–167**, 156–164.

57 E. Nikan, A. A. Khodadadi and Y. Mortazavi, *Sens. Actuators, B*, 2013, **184**, 196–204.

58 N. M. Vuong, N. M. Hieu, H. N. Hieu, H. Yi, D. Kim, Y.-S. Han and M. Kim, *Sens. Actuators, B*, 2014, **192**, 327–333.

59 Z. Karami Horastani, S. M. Sayedi, M. H. Sheikhi and E. Rahimi, *Mater. Sci. Semicond. Process.*, 2015, **35**, 38–44.

60 S. Nasresfahani, M. H. Sheikhi, M. Tohidi and A. Zarifkar, *Mater. Res. Bull.*, 2017, **89**, 161–169.

61 J. Hu, F. Gao, Z. Zhao, S. Sang, P. Li, W. Zhang, X. Zhou and Y. Chen, *Appl. Surf. Sci.*, 2016, **363**, 181–188.

62 D. Zhang, H. Chang, Y. e. Sun, C. Jiang, Y. Yao and Y. Zhang, *Sens. Actuators, B*, 2017, **252**, 624–632.